ACS NANO

www.acsnano.org



ARTICLE

# Discovery and Characterization of a Metastable Cubic Interstitial Nickel–Carbon System with an Expanded Lattice

Albert Gili,* Martin Kunz, Daniel Gaissmaier, Christoph Jung, Timo Jacob, Thomas Lunkenbein, Walid Hetaba, Kassiogé Dembélé, Sören Selve, Reinhard Schomäcker, Aleksander Gurlo,†† and Maged F. Bekheet††

Cite This: *ACS Nano* 2025, 19, 2769–2776

Read Online

ACCESS | Metrics & More | Article Recommendations | Supporting Information

**ABSTRACT:** **Metastable, *i.e.*, kinetically favored but thermodynamically not stable, interstitial solid solutions of carbon in iron are well-understood. Carbon can occupy the interstitial atoms of the host metal, altering its properties. Alloying of the host metal results in the stabilization of the $FeC_x$ phases, widening its application. Pure nickel finds niche applications, mainly focusing on catalysis, while nickel alloys are widely applied, *e.g.*, in gas turbines, reactors, and seawater piping. Nickel carbide ($Ni_3C$) is the well-known stable Ni−C system displaying a rhombohedral ($R\bar{3}c$) crystal structure. Some reports describe an elusive cubic Ni−C system, observed during certain catalytic reactions occurring on nickel and formed by the occupation of the interstitials of the metal with carbon: to date, the stabilization and characterization of this phase have not been accomplished. Hereby, we report on the synthesis of a cubic metastable $NiC_x$ phase using chemical vapor deposition of methane on supported nickel nanoparticles. The structure was predicted by DFT/ReaxFF, synthesized and monitored with *in situ* time-resolved synchrotron XRD, and experimentally confirmed by Rietveld refinement and (S)TEM-EELS under ambient conditions. The results show an $Fm\bar{3}m$ phase with a lattice parameter of $a$ = 3.749 ± 0.037 Å at room temperature, with the highest ever reported atomic percentage of carbon occupying the octahedral interstices of 23.1%, resulting in a $NiC_{0.3}$ phase. The degree of occupation of the interstitial voids by carbon can be controlled, enabling the tuning of the host metal's $d$-spacing and composition, highlighting the applicability of this synthesis route for catalytic nanoparticle preparation.**

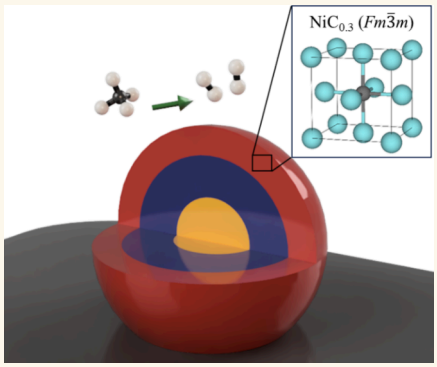


**KEYWORDS:** *solid solution, carbide, in situ XRD, TEM, nanoparticle, catalysis*



## INTRODUCTION

Iron and carbon constitute the most studied example of an interstitial solid solution: carbon can occupy the interstitials of the host iron structure, distorting its lattice.[1] Quenching leads to the (meta)stabilization of different phases like martensite ($P4/mmm$), bainite ($P4/mmm$ or $Pm\bar{3}m$), or pearlite ($Pnma$), which display distinct properties compared to simple iron. These processes have been applied for thousands of years: today, steel is one of the most used materials globally. In comparison to iron, the story of nickel and carbon is less ubiquitous.

Metallic nickel possesses a cubic structure ($Fm\bar{3}m$), whereas the known nickel carbide ($Ni_3C$) exhibits a trigonal ($R\bar{3}c$) structure with an additional ordered sublattice of interstitial carbon.[2] Several reports in the literature describe the formation of a solid solution of carbon in the cubic nickel during specific chemical processes like the chemical vapor deposition (CVD) of hydrocarbons to form carbon nanotubes/nanofibers (CNT/CNF)[3−5] or during the dry reforming of methane (DRM).[6,7] During CVD, $CH_4$ (or other C-containing precursors) decomposes to produce $H_2$ and surface carbon atoms. These can occupy the interstitial sites of the metal host, forming a solid solution and expanding the crystal's unit cell.[4,7] Graphitic CNT/CNF formation follows the exsolution of the dissolved carbon under certain conditions.[3] Understanding the carbon diffusion mechanisms and the $NiC_x$ intermediates is of key importance for rational catalyst design.[7,8] Indeed, theoretical

Received: October 28, 2024
Revised: December 21, 2024
Accepted: December 27, 2024
Published: January 6, 2025

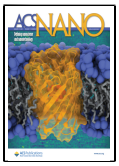

work already foresaw the existence of a metastable cubic Ni−C system in the transformation sequence from *fcc* Ni to *hcp* $Ni_3C$, predicting that carbon atomic contents above 25% in the *fcc* $Ni_4C$ would lead to instability and yield the *hcp* $Ni_3C$.[8] Experimentally, the work successfully used Au as a substrate for the growth of Ni and later carbonization to stabilize the metastable $NiC_x$ compounds due to the lattice match with the Au support.

The increasing price of noble metals combined with the unique capability of nickel to enable new catalytic pathways has stimulated interest in this transition metal for organic chemistry,[9] heterogeneous,[10] electro-,[11] and photocatalysis.[12] Using substitutional and intermetallic alloys enables engineering the electronic configuration of multimetallic catalytic nanoparticles, modifying the adsorption and reaction energies of specific catalytic pathways.[10,13,14] Besides, the inclusion of heteroatoms in the interstices of catalytic nanoparticles strongly affects the subsurface chemistry and modifies the product selectivity.[15−19] An example is hydrogenation reactions: if present, C occupies the interstitials of Pd (or $Ni_3Zn$[16]) during alkyne semihydrogenation, minimizing the population of hydrogen in the subsurface and avoiding overhydrogenation of the reaction intermediates.[20]

In this work, we report the prediction, synthesis, and characterization of supported cubic $NiC_x$ nanoparticles synthesized by CVD of $CH_4$. DFT/ReaxFF calculations predict the structure and point out the preferred occupation of octahedral interstitials. Synthesis of the $NiC_x$ structures was followed *in situ* using synchrotron X-ray diffraction (XRD). Stabilizing the interstitial alloy and anchoring carbon in the nickel nanoparticles allows further investigation of the structures at room temperature. Diffraction combined with transmission electron microscopy (TEM) and scanning transmission electron microscopy-electron energy loss spectroscopy (STEM-EELS) demonstrates the metastable presence of a cubic supersaturated $NiC_{0.3}$ phase at room temperature. The discovery of this phase encourages further investigation to be applied as a synthesis route to engineer the electronic configuration, tune the *d*-spacing, and control the subsurface chemistry of supported nickel nanoparticles for catalysis.

## RESULTS AND DISCUSSION

Figure 1 shows the obtained (Helmholtz free) energies of formation per atom for various $NiC_x$ structures at 800 °C (extended data are shown in Tables S1 and S2 and Figures S1−S3). The results show a preferential occupation of the octahedral interstitial sites (as previously predicted[21]) by C and an energetically preferred cubic $Ni_3C$. For a small number of doped carbon atoms (<$Ni_3C$), it is energetically favorable to form octahedral $Ni_xC$ structures as well. For structures with carbon content larger than that of $Ni_3C$, the space groups of the modified lattices become more stable. For the modified lattice structures of $Ni_2C$ A1 and A2, an energetically degenerate state occurs. Our results are an extension of the possible structures previously reported[8] and agree with the relative stability of $Ni_3C$ and predict its existence.

The synthesis of the predicted cubic nanoparticles of $NiC_x$/MnO was performed and monitored in situ using XRD (the reasons for using MnO as a support are clarified in the Methods section). Figure 2A shows the patterns obtained during CVD at 800 °C and posterior quenching (see Figure S4 for the initial structure after the reduction step/proof of the absence of NiO and Figure S5 for the full experiment): the

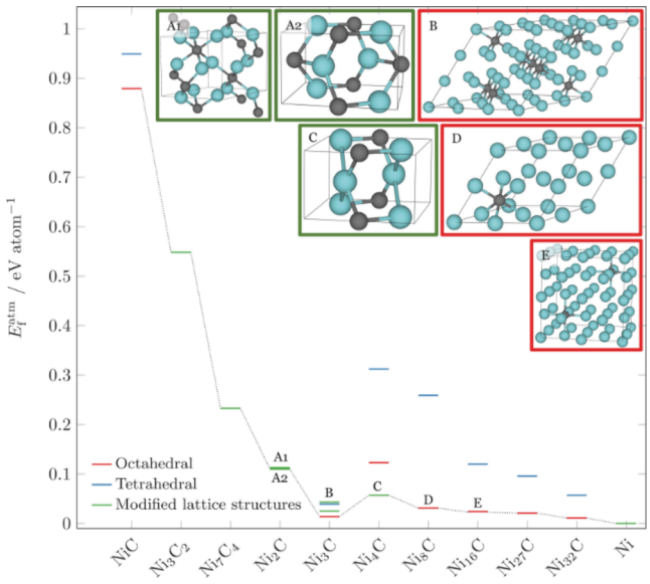


**Figure 1. Formation energies per atom ($E_f^{atm}$) obtained with DFT/ReaxFF for several $NiC_x$ in tetrahedral (blue) and octahedral (red) interstitials as well as selected modified lattice structures[22] (green) at 800 °C.**

patterns are stacked and progressively turn from black to blue (bottom up) with time on stream (TOS). Decomposition of $CH_4$ on the Ni nanoparticles at 800 °C results in the intercalation of C atoms in the octahedral interstices of the metal (in contrast to tetrahedral occupation as theoretically proven in Figure 1), expanding its unit cell as evidenced by the shift toward lower $2\theta$ of the nickel reflections.[7] Note that this expansion cannot be caused by the endothermic $CH_4$ decomposition reaction. The formation of $NiC_x$'s is due to the difference in energy barrier between $CH_4$ decomposition,[23] a reaction occurring on the external surface of the particles, and C diffusion toward the core of the nanoparticles, resulting in an onion-type multiphase structure with increasing C content from core to shell.[7] Due to the on-the-fly analysis during data acquisition, the oven was quenched (−6.5 °C·s$^{-1}$, see the Methods section) as soon as the expanded reflections were observed. The rapid drop in temperature shifts the reflections to higher angles due to thermal contraction, and even after a few minutes at room temperature, the $NiC_x$ phases remain detectable. The lack of the main graphite reflection (002) ($P6_3/mmc$, PDF No. 00-041-1487) at $2\theta$ = 8.42 (25 keV) (see Figure S5) at the end of the experiment demonstrates the absence of significant graphitic structures, suggesting the success of the quenching procedure. This procedure hinders kinetically the otherwise thermodynamically favored exsolution of C-structures upon cooling. It is worth noting that our previous works showed that the formation of graphitic carbon during the CVD process is always accompanied by the exsolution of carbon from the $NiC_x$ phases.[6,7] During the whole process, nickel and the $NiC_x$ phases maintain their cubic ($Fm\bar{3}m$) structure: the $R\bar{3}c$ structure belonging to $Ni_3C$ remains undetectable. The lattice parameter obtained by Rietveld refinement of the *in situ* data (Figure 2A) *vs* TOS is shown in Figure 2B: at room temperature, $NiC_{x3}$ displays a value of 3.7753(7) Å, $NiC_{x2}$ displays a value of 3.6943(7) Å, and $NiC_{x1}$ displays a value of 3.5844(15) Å. An estimation of the carbon content can be obtained by combining experimental values of lattice parameters and the ReaxFF


https://doi.org/10.1021/acsnano.4c15300
ACS Nano 2025, 19, 2769−2776

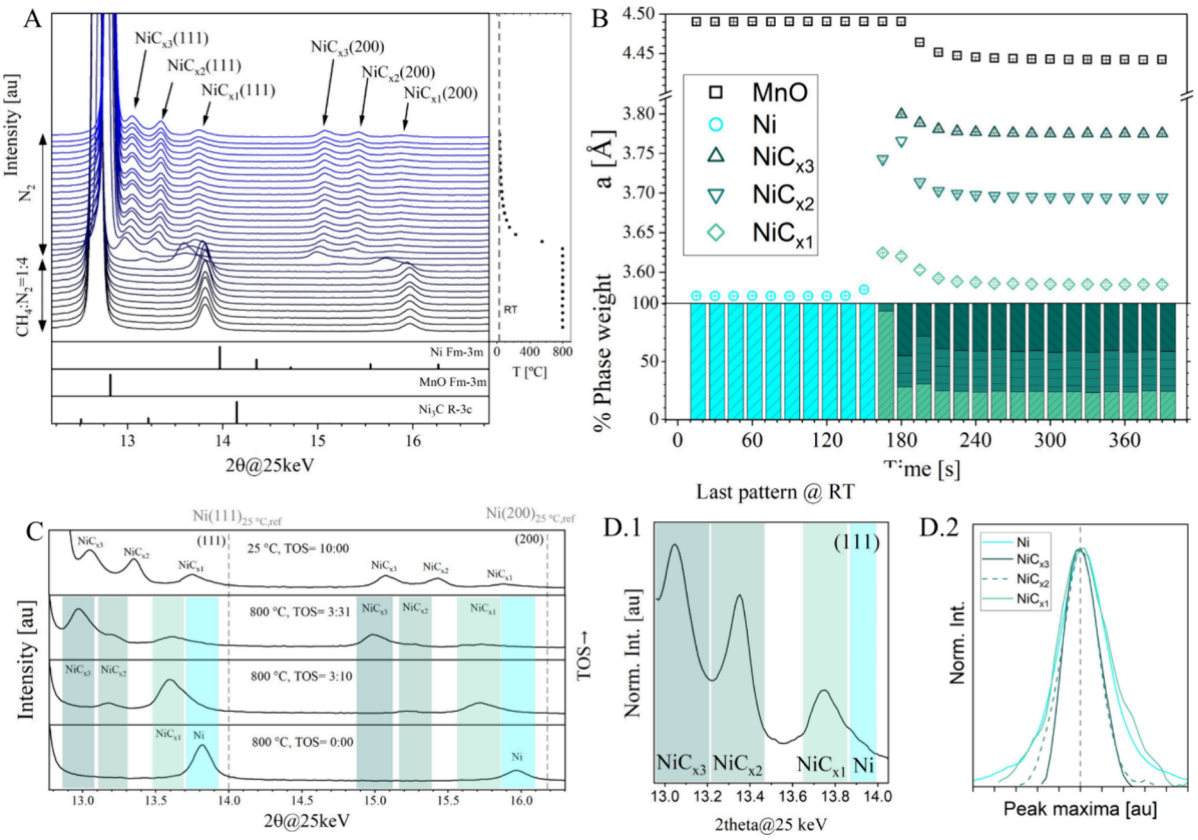


**Figure 2. Phase evolution of the Ni and $NiC_x$ phases from *in situ* XRD during the CVD of $CH_4$. Panel (A) shows the evolution of the Ni/$NiC_x$(111) and (200) reflections: the stacked patterns evolve from black to blue with TOS. Reference graphs belong to Ni (*Fm*$\bar{3}$*m*, 00-004-0850), MnO (*Fm*$\bar{3}$*m*, 01-088-0424), and $Ni_3C$ (*R*$\bar{3}$*c*, 01-072-1467). Panel (B) shows the lattice parameter and weight fraction of the Ni-containing phases (relative to the Ni-containing phases exclusively) as a function of the TOS obtained by Rietveld refinement. Panel (C) displays a magnification of the Ni(111) and (200) zones of selected patterns. Panel (D.1) shows the individually normalized intensity of the $NiC_{x1-3}$ (111) reflection of the last pattern at RT. Panel (D.2) shows the comparison of peak shape of the (111) reflections of Ni (800 °C) and the $NiC_x$ (last pattern, RT, the same as D.1). The reflections' maxima are displaced and the intensity normalized to allow for shape comparison.**

simulations, as previously done.[7] Thus, phase compositions of $NiC_{0.30}$ ($NiC_{x3}$), $NiC_{0.24}$ ($NiC_{x2}$), and $NiC_{0.05}$ ($NiC_{x1}$) are obtained. The carbon content of all these compounds is above the experimental limit of solubility in bulk nickel[23]; hence the term supersaturated. It is worth noting that the estimated lattice parameter of the cubic $NiC_x$ phase reported by Kang et al.[8] was 3.637(5), lower than those of the $NiC_{x3}$ and $NiC_{x2}$ reported in this work. Therefore, the maximum solubility of C in the *fcc* lattice of Ni is experimentally observed in the structures reported here. The relative weight percentage of each Ni-containing phase obtained from refinement is shown at the bottom of Figure 2B, highlighting the total disappearance of metallic nickel and the major fraction of $NiC_{x3}$ (the most external $NiC_x$). The symmetry of the $NiC_x$ reflections changes compared to that of metallic Ni. The shift of the peak maxima's position is related to the expansion of the unit cell caused by the intercalation of C: lower 2Θ angle means more expanded cell, *i.e.*, more C in the $NiC_x$ structure. Figure 2D.2 shows the Ni (at 800 °C before the CVD process) and the $NiC_x$ (last pattern@RT) normalized (111) reflections (in both intensity and peak maxima position). The $NiC_{x1}$ reflection exhibits a very similar peak shape compared to that of Ni, with very similar Gaussian and Lorentzian integral breadths but with the appearance of an asymmetric shoulder right of the maxima: this is most probably created by the existence of a solid-solution gradient to lower C-contents or even by the presence of "unreacted" metallic Ni. Note that the presence of a solid-solution gradient results in a Gaussian-type of broadening, similar to that of microstrain.[24] A similar shoulder is observed left of the maxima of the $NiC_{x2}$ reflection, which could be caused again by the presence of a solid-solution gradient. A decrease of the Lorentzian integral breadth in the $NiC_{x2}$ and $NiC_{x3}$ compared to the initial Ni is most probably caused by crystallite size growth: the presence of defects like dislocations, twin faults, stacking faults, and layer mistakes would induce Lorentzian broadening to the peak shape, which is not observed in our experiment. The sample was recovered for characterization with TEM.

Figure 3 shows the morphological and chemical characterization of the samples performed using TEM and EELS (other nanoparticles and scales shown in Figure S6). The findings highlight the absence of CNTs/CNFs (Figure S6A). Most of the nickel nanoparticles display a thin graphitic structure (Figure 3A.1), as indicated by its interplanar distance $d_{(002)}$ of ~0.335 nm, or an amorphous carbon (Figure S6B1,B2) layer covering their outer surface, most probably generated upon minor carbon exsolution during quenching.[5,25] A few graphitic structures can be observed, as evidenced by selected area electron diffraction (SAED, Figure S7). An image of $NiC_x$/MnO is shown in Figure 3A.1. The corresponding fast Fourier


https://doi.org/10.1021/acsnano.4c15300
ACS Nano 2025, 19, 2769−2776

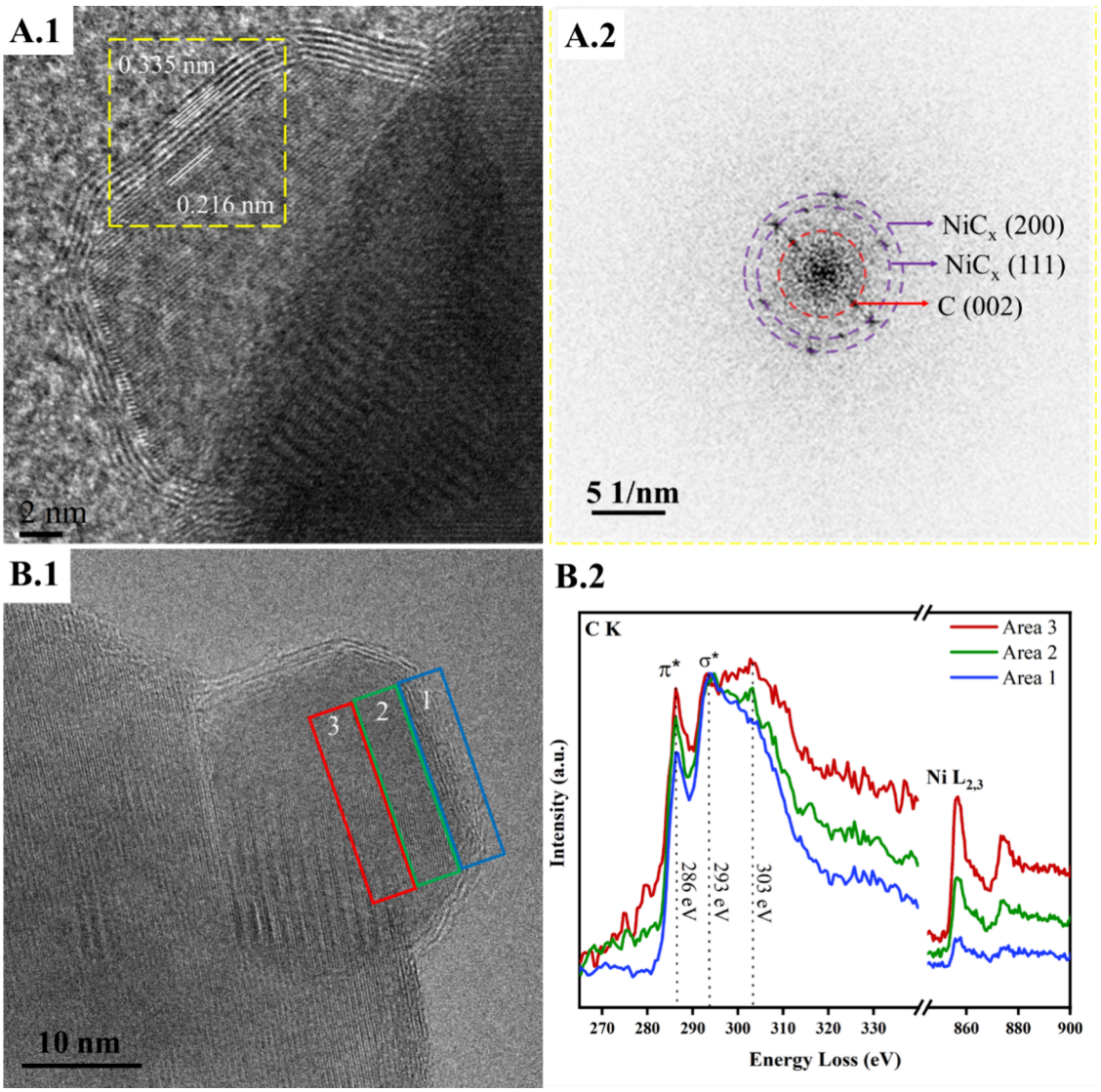


**Figure 3. Structural and chemical characterizations with TEM-STEM/EELS. (A.1) HR-TEM image of a NiC$_x$ sample with an interplanar distance obtained from FFT. (A.2) FFT on the inset in (A.1), with interplanar distances belonging to C(002) = 0.335 nm, NiC$_x$(111) = 0.216 nm, and NiC$_x$(200) = 0.185 nm. (B.1) TEM image showing a nanoparticle with a carbon encapsulating layer and 3 zones of analysis with EELS. (B.2) EELS spectra of image B.1, showing the nickel and carbon edge of the three areas depicted in (B.1). The EEL spectra were Fourier ratio deconvolved to remove the effects of plural scattering.**

transform (FFT, Figure 3A.2) shows an interplanar distance of 0.216 nm, characteristic of the (111) plane of the supported $NiC_{0.3}$ or $NiC_{0.24}$ phases (see Table S4). This *d*-spacing is 6.2% above the reported value for metallic nickel (PDF No. 00−004−0850), highlighting the expanded cell. Calculation of the lattice parameter of this value leads to $a$ = 3.741 Å, in good agreement with values obtained from refinement of the XRD data. STEM-EELS analysis of a typical NiC$_x$ (Figure 3B2) particle allows determining qualitative changes in the carbon content and the structure of nickel along the radial direction of the particle (colored areas in Figure 3B.1). There is an increase of the C/Ni ratio in the radial direction from core to shell, most probably caused by the encapsulation of the particle by graphitic carbon and/or the increase of the C content in the NiC$_x$ phase. The $\sigma^*/\pi^*$ ratio of the C signal increases in the radial direction from core to shell, which could be related to an increase in the C concentration in the NiC$_x$ phase. However, its interpretation is not straightforward as carbon is known for its anisotropicity and the ratio can change if the carbon structure is oriented differently to the electron beam. A peak at 303 eV is observed in areas 3 and 2, which decreases from core to shell. A similar peak has been previously reported at energy losses of 302 and 305 eV and has been attributed to carbide formation in the $Al_2MgC_2$ system.[26] An additional proof of the formation of a solid solution of C in Ni evolves from the comparison of the Ni $L_{2,3}$-edge acquired on a NiC$_x$ sample and a Ni-metal reference sample (Figure S8). The spectrum of the NiC$_x$ sample is shifted 1 eV toward higher energy losses compared to the spectrum of the Ni-metal. The same shift was previously observed in Ni 2p XPS[5] and in the Fe $L_{2,3}$ electron energy-loss edge of iron carbide.[27]

The NiC$_x$ structures are metastable: Figure S9 shows a nanoparticle from another experiment performed with the same material and procedure but quenched before the maximal expansion was achieved. The original particle (Figure S9A.1,B) shows the absence/a very thin carbon external shell, and *d*-spacings ∼5% expanded compared to the reference Ni. During observation in the microscope, the particle shrunk (from a


https://doi.org/10.1021/acsnano.4c15300
ACS Nano 2025, 19, 2769−2776

diameter of 33.33 to 28.63 nm, relative shrinkage of 14.1%), and an external shell of approximately 4.79 nm amorphous C was formed. This phenomenon was caused by the electron beam, which resulted in the exsolution of the C dissolved from the interstitials of the Ni nanoparticle.

Previous observations of similar *fcc* $NiC_x$ phases were reported,[5] but recovery and characterization are done for the first time in this work. We envision the methodology described here as a tool to produce supported metal nanoparticles with an engineered electronic configuration, lattice parameter, and tailored subsurface chemistry. The application of such systems (including nickel and some nickel-containing alloys as starting supported nanoparticles) has great potential for heterogeneous, electro-, and photocatalysis. Indeed, some notorious cases have already been reported.[16] The catalyst support can be modified to adapt to specific catalytic systems, while several methods can be applied to impregnate controlled-sized metal nanoparticles. The size of the initial particles strongly affects the carbon solubility limit[28] and, as a consequence, the final composition, lattice parameter, and electronic configuration. Through precise control of the CVD conditions applied, namely, carbon-precursor type, flow and partial pressure, temperature,[7] and exposure time, specific structures can be obtained.

## CONCLUSIONS

We report on the prediction of a $NiC_x$ $Fm\bar{3}m$ structure using DFT/ReaxFF, its synthesis in supported nanoparticulate form using time-resolved synchrotron-based *in situ* XRD, and the later *ex situ* characterization using electron microscopy. Theoretical and experimental results show a *fcc* Ni crystal structure with C atoms occupying the octahedral interstitials to yield metastable $NiC_{0.3}$. The thorough characterization of this phase is done for the first time; we envision the suggested methodology as a pathway to create supported metal nanoparticles with tailored composition, lattice parameter, and subsurface chemistry.

## METHODS

**5% Ni/MnO Synthesis.** A procedure previously reported in ref 6 was followed. Briefly, the $NiO/MnO_x$ catalyst precursor was synthesized using the coprecipitation method. An aqueous solution containing the proper amounts of nickel acetate tetrahydrate ($Ni(OCOCH_3)_2{\cdot}2H_2O$) and manganese nitrate tetrahydrate ($Mn(NO_3)_2{\cdot}4H_2O$) was mixed under stirring with an aqueous solution of $NaHCO_3$ and NaOH with a pH $\geq$ 10 to induce precipitation. The resulting solid was dried at 80 °C and subsequently calcined for 4 h at 750 °C. To achieve the catalyst during the in situ XRD analysis, a flow of pure $H_2$ (GHSV = 54,000 L $h^{-1}$ $kg_{cat}^{-1}$) was applied at 500 °C. The reduction of the $MnO_x$ support results in the exsolution of metallic nickel nanoparticles which decorate the surface of the MnO support. The reasons for the use of MnO as a support are (i) to produce exsoluted Ni nanoparticles with controlled size and (ii) due to the previous application of the catalyst to the dry reforming of methane,[6,7] studies which initiated the present work. MnO is inert for $CH_4$ decomposition.

**Characterization.** In situ XRD experiments were performed on beamline 12.2.2 of the Advanced Light Source (ALS) synchrotron facility in Berkeley, CA, USA. The setup and technique details have been previously described in refs 29−31. Shortly, a set of mass flow controllers allow controlling the flow rate and composition of the gas stream. Around 1 mg of the powder sample is contained inside a quartz capillary and assembled into the setup. Gas delivery occurs by using a tungsten carbide filament. The reaction temperature is controlled with an S-type thermocouple and using two IR lamps connected to a PID controller *via* Labview software. A 2D PerkinElmer detector allows for acquiring high-quality patterns using short acquisition times. A typical experiment consists of (i) heating steps ($N_2$ flow, 1 °C·$s^{-1}$), (ii) the reduction step to reduce the $NiO/Mn_2O_3$ solid solution to produce Ni/MnO (1 N mL·$min^{-1}$ flow of $H_2$, see Figure S4 for structural information: Ni is in metallic form at the beginning of the experiment, no NiO could be detected), the $CH_4$ decomposition (800 °C, reactant mixture of $CH_4$:$N_2$ = 1:4 and GHSV of 60,000 L $h^{-1}$ $kg_{cat}^{-1}$, time 0:00 belongs to the injection of $CH_4$ in the gas feed) using 5% Ni/MnO as a material precursor to yield the $NiC_x$/MnO compound, and (iv) the final quenching. In order to quench the sample and immobilize the carbon content, short acquisition times of 20 s $pattern^{-1}$ were used to observe changes in the position of the nickel (111) and (200) reflections while analyzing the data "on-the-fly" using Dioptas software. When the reflection shift was observed, the oven power supply was interrupted (set to 0), and the reactant flow rate was stopped while continuously acquiring patterns. Applying this methodology and for the experiments reported, the cooling rate was approximately −6.5 °C $s^{-1}$ between 800 and 100 °C. The cooling rate was nonlinear due to the difficulty in removing heat from the setup at lower temperatures due to the decreased temperature gradient between the SiC tube and the air. At room temperature, pure $N_2$ was flushed through the sample, and the sample was recovered in an inert gas for later microscopy characterization. Rietveld refinement of the XRD data was performed using FullProf Suite software[32] and fitting using a Thompson−Cox−Hastings pseudo-Voigt function[33] with an axial divergence asymmetry function[34] (Function 7). The sample-to-detector distance for integration and the instrument resolution function for refining were obtained by using a $LaB_6$ NIST 660c standard.

*Ex situ* TEM was performed by using two different microscopes. First, a JEOL microscope (JEM-ARM200 CF) operating at 200 kV and equipped with a cold field emission gun (CFEG) and a double Cs corrector for TEM and STEM imaging modes was used. STEM images were acquired using a Gatan high-angle annular dark-field (HAADF) and bright field (BF) detectors, with a probe size of 1.5 nm and a current of 1 nA. STEM-EELS data were acquired using a Gatan imaging filter (GIF) spectrometer (model quantum) with a beam convergence semiangle of 22.8 mrad, a collection semiangle of 54.5 mrad, and a dispersion energy of 0.5 eV per channel. The current was set between $2 \times 10^7$ and $9 \times 10^7$ e/s, which was verified by using a Faraday cup holder. Second, an image Cs-corrected HR-TEM (FEI Titan 80−300 Berlin Holography Special) microscope with XFEG operated at 300 kV was used. Under the conditions applied in Figure S9, the calculated electron dose rate was $3.3 \times 10^9$ electron·$s^{-1}$, with the overall dosage on the very particle between both images being $1.4 \times 10^{13}$.

**DFT Calculations.** First-principles calculations have been performed using the Vienna Ab initio Simulation Package (VASP).[35,36] The projector augmented wave (PAW) method[37] in the implementation of Kresse and Joubert[35] was applied for an accurate and efficient calculation of the system's electronic structure. Exchange correlation effects were described by the Bayesian error estimation functional with van der Waals (BEEF-vdW)[38] in the framework of the generalized gradient approximation (GGA). According to the scheme of Monkhorst and Pack, a *k*-point mesh density of 0.15 $Å^{-1}$ was used to sample the Brillouin zone (BZ). For an accurate expansion of the one-particle electron wave functions into a plane-wave basis set, a cutoff energy of 750 eV was chosen. The calculations were considered to be converged once the total energy difference was less than $1 \times 10^{-7}$ eV and the norms of all the forces were smaller than $1 \times 10^{-4}$ eV $Å^{-1}$. After intensive testing, the reactive force field (ReaxFF) of Mueller et al.[39] was used to determine the entropic contributions. All ReaxFF[40,41] calculations were performed within the ReaxFF implementation of the Amsterdam Modeling Suite 2019.[42] The contributions for the respective systems were calculated within the ASE Phonon module framework.[43,44] Each cell was repeated three times in all spatial directions to minimize the influence of the periodic images, and a displacement value of 0.01 Å for the small displacement method was applied.



https://doi.org/10.1021/acsnano.4c15300
ACS Nano 2025, 19, 2769−2776

The formation energies per formula unit (f.u.) and atom (atm) were calculated by

$$E_f^{f.u.} = E_{Ni_xC_y} - x \cdot E_{Ni}^{bulk} - y \cdot E_C^{Graphite} \quad (1)$$

and

$$E_f^{atm} = \frac{1}{x+y}(E_{Ni_xC_y} - x \cdot E_{Ni}^{bulk} - y \cdot E_C^{Graphite}) \quad (2)$$

where $E_{Ni_xC_y}$ is the total energy of the Ni−C bulk system, $E_{Ni}^{bulk}$ is the total energy per atom of *fcc*-Ni, and $E_C^{Graphite}$ is the energy of a single C atom in graphite. Internal energy components $U$ at $T$ = 1073 K have been calculated from the sum of the system's potential energy $E_{pot}$, zero-point energy $E_{ZPE}$, and phonon energy contribution $E_{Phonon}$ using the following equation:

$$U = E_{pot} + E_{ZPE} + E_{Phonon} \quad (3)$$

The Helmholtz free energy at $T$ = 1073 K was then determined by

$$F = U - T \cdot S \quad (4)$$

where $S$ is the entropy contribution.

All studied structures are provided as POSCAR files in the Supporting Information.

## ASSOCIATED CONTENT

### Supporting Information

The Supporting Information is available free of charge at https://pubs.acs.org/doi/10.1021/acsnano.4c15300.

Summary of the calculated formation energies; schematic illustration of the studied octahedral Ni−C bulk cells; schematic illustration of the studied tetrahedral nickel $NiC_x$ bulk cells; schematic illustration of the studied modified nickel $NiC_x$ lattice structures; summary of the calculated zero-point energy values, energy contribution of the phonons, internal energy values, entropy contributions, and formation energy values; *in situ* XRD patterns of the reduction step; *in situ* XRD patterns of the full CVD experiment; TEM images; SAED analysis; EELS comparison of the Ni $L_{2,3}$-edge acquired on a $NiC_x$ particle and a Ni-metal reference sample; Ni, C (graphite), and MnO plane distances with corresponding hkl indexes; and comparison of experimental interplanar distances obtained by TEM imaging and XRD-RR analysis (PDF)

## AUTHOR INFORMATION


### Corresponding Author

**Albert Gili** − *Faculty III Process Sciences, Institute of Materials Science and Technology, Chair of Advanced Ceramic Materials, Technische Universität Berlin, 10623 Berlin, Germany; Institut für Chemie, Technische Universität Berlin, 10623 Berlin, Germany; Helmholtz-Zentrum Berlin für Materialien und Energie, 14109 Berlin, Germany; Advanced Light Source, Lawrence Berkeley National Laboratory, Berkeley, California 94720, United States;* orcid.org/0000-0001-7944-7881; Email: albert.gili@helmholtz-berlin.de

### Authors

**Martin Kunz** − *Advanced Light Source, Lawrence Berkeley National Laboratory, Berkeley, California 94720, United States*

**Daniel Gaissmaier** − *Institute of Electrochemistry, Ulm University, 89081 Ulm, Germany; Helmholtz-Institute Ulm (HIU) Electrochemical Energy Storage, 89081 Ulm, Germany; Karlsruhe Institute of Technology (KIT), 76021 Karlsruhe, Germany;* orcid.org/0000-0002-7688-1989

**Christoph Jung** − *Institute of Electrochemistry, Ulm University, 89081 Ulm, Germany; Helmholtz-Institute Ulm (HIU) Electrochemical Energy Storage, 89081 Ulm, Germany; Karlsruhe Institute of Technology (KIT), 76021 Karlsruhe, Germany*

**Timo Jacob** − *Institute of Electrochemistry, Ulm University, 89081 Ulm, Germany; Helmholtz-Institute Ulm (HIU) Electrochemical Energy Storage, 89081 Ulm, Germany; Karlsruhe Institute of Technology (KIT), 76021 Karlsruhe, Germany;* orcid.org/0000-0001-7777-2306

**Thomas Lunkenbein** − *Department of Inorganic Chemistry, Fritz-Haber-Institut der Max-Planck-Gesellschaft, 14195 Berlin, Germany;* orcid.org/0000-0002-8957-4216

**Walid Hetaba** − *Abteilung Heterogene Reaktionen, Max-Planck-Institut für chemische Energiekonversion, 45470 Mülheim an der Ruhr, Germany*

**Kassiogé Dembélé** − *Department of Inorganic Chemistry, Fritz-Haber-Institut der Max-Planck-Gesellschaft, 14195 Berlin, Germany*

**Sören Selve** − *Center for Electron Microscopy (ZELMI), Technische Universität Berlin, 10623 Berlin, Germany*

**Reinhard Schomäcker** − *Institut für Chemie, Technische Universität Berlin, 10623 Berlin, Germany;* orcid.org/0000-0003-3106-3904

**Aleksander Gurlo** − *Faculty III Process Sciences, Institute of Materials Science and Technology, Chair of Advanced Ceramic Materials, Technische Universität Berlin, 10623 Berlin, Germany*

**Maged F. Bekheet** − *Faculty III Process Sciences, Institute of Materials Science and Technology, Chair of Advanced Ceramic Materials, Technische Universität Berlin, 10623 Berlin, Germany;* orcid.org/0000-0003-1778-0288

Complete contact information is available at: https://pubs.acs.org/10.1021/acsnano.4c15300


### Author Contributions

[††]A.Gu. and M.F.B. contributed equally. A.Gi. performed conceptualization, data curation, formal analysis, investigation, and writing of the manuscript; M.K. performed the investigation and methodology; D.G. performed the formal analysis, investigation, methodology, and review of the work; T.J. did the formal analysis, investigation, methodology, review, and the project administration; T.L. did the review and the project administration; W.H. performed data evaluation and reviewed the manuscript; K.D. did the investigation and methodology; S.S. did the investigation and reviewed the manuscript; R.S. did the project administration, resources, supervision and reviewed the manuscript; A.Gu. did the conceptualization, project administration, resources, supervision and review of the manuscript; M.F.B. performed the conceptualization, data curation, formal analysis, methodology, and writing the manuscript.

### Notes

The authors declare no competing financial interest.

## ACKNOWLEDGMENTS

A.Gi. and T.L. acknowledge support from the German Federal Ministry of Education and Research in the framework of the project Catlab (03EW0015A/B). A.Gi. and W.H. appreciate

the support of Unifying Systems in Catalysis (UniSysCat), funded by the Deutsche Forschungsgemeinschaft (DFG, German Research Foundation) under Germany's Excellence Strategy—EXC 2008/1-390540038. This research used resources of the Advanced Light Source, which is a DOE Office of Science User Facility under contract no. DE-AC02-05CH11231. Part of this work was funded by the Deutsche 429 Forschungsgemeinschaft DFG (TRR234 "CataLight", Projects A5 and B10). Further, this work was partially supported by the state of Baden-Württemberg through bwHPC and the German Research Foundation (DFG) under Grant No. INST 40/575-1 FUGG (JUSTUS 2 cluster).

## ABBREVIATIONS

CVD, chemical vapor deposition; CNF, carbon nanofiber; CNT, carbon nanotube; EELS, electron energy loss spectroscopy; TEM, transmission electron microscopy; STEM, scanning transmission electron microscopy; SAED, selected area electron diffraction

## REFERENCES

(1) Hume-Rothery, W. Some notes on the structures of alloys of iron. *Contemp. Phys.* **1964**, *5* (5), 321–347.
(2) Bayer, B. C.; Bosworth, D. A.; Michaelis, F. B.; Blume, R.; Habler, G.; Abart, R.; Weatherup, R. S.; Kidambi, P. R.; Baumberg, J. J.; Knop-Gericke, A.; Schloegl, R.; Baehtz, C.; Barber, Z. H.; Meyer, J. C.; Hofmann, S. In Situ Observations of Phase Transitions in Metastable Nickel (Carbide)/Carbon Nanocomposites. *J. Phys. Chem. C* **2016**, *120* (39), 22571–22584.
(3) Helveg, S.; Lopez-Cartes, C.; Sehested, J.; Hansen, P. L.; Clausen, B. S.; Rostrup-Nielsen, J. R.; Abild-Pedersen, F.; Nørskov, J. K. Atomic-scale imaging of carbon nanofibre growth. *Nature* **2004**, *427*, 426–429.
(4) Hofmann, S.; Sharma, R.; Ducati, C.; Du, G.; Mattevi, C.; Cepek, C.; Cantoro, M.; Pisana, S.; Parvez, A.; Cervantes-Sodi, F.; Ferrari, A. C.; Dunin-Borkowski, R.; Lizzit, S.; Petaccia, L.; Goldoni, A.; Robertson, J. In situ observations of catalyst dynamics during surface/bound carbon nanotube nucleation. *Nano Lett.* **2007**, *3* (3), 602–608.
(5) Rinaldi, A.; Tessonnier, J.-P.; Schuster, M. E.; Blume, R.; Girgsdies, F.; Zhang, Q.; Jacob, T.; Abd Hamid, S. B.; Su, D. S.; Schlögl, R. Dissolved carbon controls the initial stages of nanocarbon growth. *Angew. Chem., Int. Ed. Engl.* **2011**, *50* (14), 3313–3317.
(6) Gili, A.; Schlicker, L.; Bekheet, M. F.; Görke, O.; Penner, S.; Grünbacher, M.; Götsch, T.; Littlewood, P.; Marks, T. J.; Stair, P. C.; Schomäcker, R.; Doran, A.; Selve, S.; Simon, U.; Gurlo, A. Surface Carbon as a Reactive Intermediate in Dry Reforming of Methane to Syngas on a 5% Ni/MnO Catalyst. *ACS Catal.* **2018**, *8*, 8739–8750.
(7) Gili, A.; Schlicker, L.; Bekheet, M.; Görke, O.; Kober, D.; Simon, U.; Littlewood, P.; Schomäcker, R.; Doran, A.; Gaissmaier, D.; Jacob, T.; Selve, S.; Gurlo, A. Revealing the Mechanism of Multiwalled Carbon Nanotube Growth on Supported Nickel Nanoparticles by In situ Synchrotron X-ray Diffraction, Density Functional Theory, and Molecular Dynamics Simulations. *ACS Catal.* **2019**, *9*, 6999–7011.
(8) Kang, J.-X.; Zhang, D.-F.; Guo, G.-C.; Yu, H.-J.; Wang, L.-H.; Huang, W.-F.; Wang, R.-Z.; Guo, L.; Han, X.-D. Au Catalyzed Carbon Diffusion in Ni:A Case of Lattice Compatibility Stabilized Metastable Intermediates. *Adv. Funct. Mater.* **2018**, *28* (21), No. 1706434.
(9) Ananikov, V. P. Nickel: The "Spirited Horse" of Transition Metal Catalysis. *ACS Catal.* **2015**, *5* (3), 1964–1971.
(10) Studt, F.; Abild-Pedersen, F.; Bligaard, T.; Sørensen, R. Z.; Christensen, C. H.; Nørskov, J. K. Identification of non-precious metal alloy catalysts for selective hydrogenation of acetylene. *Science* **2008**, *320* (5881), 1320–1322.
(11) Le Goff, A.; Artero, V.; Jousselme, B.; Tran, P. D.; Guillet, N.; Métayé, R.; Fihri, A.; Palacin, S.; Fontecave, M. From hydrogenases to noble metal-free catalytic nanomaterials for $H_2$ production and uptake. *Science* **2009**, *326* (5958), 1384–1387.
(12) Zhou, L.; Swearer, D. F.; Zhang, C.; Robatjazi, H.; Zhao, H.; Henderson, L.; Dong, L.; Christopher, P.; Carter, E. A.; Nordlander, P.; Halas, N. J. Quantifying hot carrier and thermal contributions in plasmonic photocatalysis. *Science* **2018**, *362* (6410), 69–72.
(13) Studt, F.; Sharafutdinov, I.; Abild-Pedersen, F.; Elkjær, C. F.; Hummelshøj, J. S.; Dahl, S.; Chorkendorff, I.; Nørskov, J. K. Discovery of a Ni-Ga catalyst for carbon dioxide reduction to methanol. *Nat. Chem.* **2014**, *6* (4), 320–324.
(14) Levy, R. B.; Boudart, M. Platinum-like behavior of tungsten carbide in surface catalysis. *Science* **1973**, *181* (4099), 547–549.
(15) Armbrüster, M.; Behrens, M.; Cinquini, F.; Föttinger, K.; Grin, Y.; Haghofer, A.; Klötzer, B.; Knop-Gericke, A.; Lorenz, H.; Ota, A.; Penner, S.; Prinz, J.; Rameshan, C.; Révay, Z.; Rosenthal, D.; Rupprechter, G.; Sautet, P.; Schlögl, R.; Shao, L.; Szentmiklósi, L.; Teschner, D.; Torres, D.; Wagner, R.; Widmer, R.; Wowsnick, G. How to Control the Selectivity of Palladium-based Catalysts in Hydrogenation Reactions: The Role of Subsurface Chemistry. *ChemCatChem.* **2012**, *4* (8), 1048–1063.
(16) Niu, Y.; Huang, X.; Wang, Y.; Xu, M.; Chen, J.; Xu, S.; Willinger, M.-G.; Zhang, W.; Wei, M.; Zhang, B. Manipulating interstitial carbon atoms in the nickel octahedral site for highly efficient hydrogenation of alkyne. *Nat. Commun.* **2020**, *11* (1), 3324.
(17) Xu, J.; Saeys, M. Improving the coking resistance of Ni-based catalysts by promotion with subsurface boron. *J. Catal.* **2006**, *242* (1), 217–226.
(18) Chan, C. W. A.; Mahadi, A. H.; Li, M. M.-J.; Corbos, E. C.; Tang, C.; Jones, G.; Kuo, W. C. H.; Cookson, J.; Brown, C. M.; Bishop, P. T.; Tsang, S. C. E. Interstitial modification of palladium nanoparticles with boron atoms as a green catalyst for selective hydrogenation. *Nat. Commun.* **2014**, *5*, 5787.
(19) Nerl, H. C.; Plodinec, M.; Götsch, T.; Skorupska, K.; Schlögl, R.; Jones, T. E.; Lunkenbein, T. In Situ Formation of Platinum-Carbon Catalysts in Propane Dehydrogenation. *Angew. Chem., Int. Ed.* **2024**, *63* (24), No. e202319887.
(20) Teschner, D.; Borsodi, J.; Wootsch, A.; Révay, Z.; Hävecker, M.; Knop-Gericke, A.; Jackson, S. D.; Schlögl, R. The roles of subsurface carbon and hydrogen in palladium-catalyzed alkyne hydrogenation. *Science* **2008**, *320* (5872), 86–89.
(21) Siegel, D. J.; Hamilton, J. C. First-principles study of the solubility, diffusion, and clustering of C in Ni. *Phys. Rev. B* **2003**, *68* (9), 344.
(22) Gibson, J. S.; Uddin, J.; Cundari, T. R.; Bodiford, N. K.; Wilson, A. K. First-principle study of structure and stability of nickel carbides. *J. Phys.: Condens. Matter.* **2010**, *22* (44), 445503.
(23) Hofmann, S.; Csányi, G.; Ferrari, A. C.; Payne, M. C.; Robertson, J. Surface diffusion:The low activation energy path for nanotube growth. *Phys. Rev. Lett.* **2005**, *95* (3), 36101.
(24) Ortiz, A. L.; Shaw, L. X-ray diffraction analysis of a severely plastically deformed aluminum alloy. *Acta Mater.* **2004**, *52* (8), 2185–2197.
(25) Batzill, M. The surface science of graphene:Metal interfaces, CVD synthesis, nanoribbons, chemical modifications, and defects. *Surf. Sci. Rep.* **2012**, *67* (3–4), 83–115.
(26) Feldhoff, A.; Pippel, E.; Wolterdorf, J. Interface Engineering of Carbon-Fiber Reinforced Mg-Al Alloys. *Adv. Eng. Mater.* **2000**, *2* (8), 471–480.
(27) Jin, Y.; Xu, H.; Datye, A. K. Electron energy loss spectroscopy (EELS) of iron Fischer–Tropsch catalysts. *Microsc. Microanal.* **2006**, *12* (2), 124–134.
(28) Diarra, M.; Zappelli, A.; Amara, H.; Ducastelle, F.; Bichara, C. Importance of carbon solubility and wetting properties of nickel nanoparticles for single wall nanotube growth. *Phys. Rev. Lett.* **2012**, *109* (18), No. 185501.
(29) Kunz, M.; MacDowell, A. A.; Caldwell, W. A.; Cambie, D.; Celestre, R. S.; Domning, E. E.; Duarte, R. M.; Gleason, A. E.; Glossinger, J. M.; Kelez, N.; Plate, D. W.; Yu, T.; Zaug, J. M.; Padmore, H. A.; Jeanloz, R.; Alivisatos, A. P.; Clark, S. M. A beamline


https://doi.org/10.1021/acsnano.4c15300
*ACS Nano* 2025, 19, 2769–2776

for high-pressure studies at the Advanced Light Source with a superconducting bending magnet as the source. *J. Synchrotron Radiat.* **2005**, *12* (Pt 5), 650−658.
(30) Doran, A.; Schlicker, L.; Beavers, C. M.; Bhat, S.; Bekheet, M. F.; Gurlo, A. Compact low power infrared tube furnace for in situ X-ray powder diffraction. *Rev. Sci. Instrum.* **2017**, *88* (1), No. 013903.
(31) Schlicker, L.; Doran, A.; Schneppmüller, P.; Gili, A.; Czasny, M.; Penner, S.; Gurlo, A. Transmission in-situ and operando high temperature X-ray powder diffraction in variable gaseous environments. *Rev. Sci. Instrum.* **2018**, *89* (3), No. 033904.
(32) Bekheet, M. F.; Grünbacher, M.; Schlicker, L.; Gili, A.; Doran, A.; Epping, J. D.; Gurlo, A.; Klötzer, B.; Penner, S. On the structural stability of crystalline ceria phases in undoped and acceptor-doped ceria materials under in situ reduction conditions. *CrystEngComm* **2019**, *38*, 145.
(33) Thompson, P.; Cox, D. E.; Hastings, J. B. Rietveld refinement of Debye−Scherrer synchrotron X-ray data from $Al_2O_3$. *J. Appl. Crystallogr.* **1987**, *20* (2), 79−83.
(34) Finger, L. W.; Cox, D. E.; Jephcoat, A. P. A correction for powder diffraction peak asymmetry due to axial divergence. *J. Appl. Crystallogr.* **1994**, *27* (6), 892−900.
(35) Kresse, G.; Joubert, D. From ultrasoft pseudopotentials to the projector augmented-wave method. *Phys. Rev. B* **1999**, *59* (3), 1758−1775.
(36) Kresse, G.; Furthmüller, J. Efficient iterative schemes for ab initio total-energy calculations using a plane-wave basis set. *Phys. Rev. B* **1996**, *54* (16), 11169−11186.
(37) Blöchl, P. E. Projector augmented-wave method. *Phys. Rev. B* **1994**, *50* (24), 17953−17979.
(38) Wellendorff, J.; Lundgaard, K. T.; Møgelhøj, A.; Petzold, V.; Landis, D. D.; Nørskov, J. K.; Bligaard, T.; Jacobsen, K. W. Density functionals for surface science: Exchange-correlation model development with Bayesian error estimation. *Phys. Rev. B* **2012**, *85* (23), No. 235149.
(39) Mueller, J. E.; van Duin, A. C. T.; Goddard, W. A. Development and Validation of ReaxFF Reactive Force Field for Hydrocarbon Chemistry Catalyzed by Nickel. *J. Phys. Chem. C* **2010**, *114* (11), 4939−4949.
(40) van Duin, A. C. T.; Dasgupta, S.; Lorant, F.; Goddard, W. A. ReaxFF: A Reactive Force Field for Hydrocarbons. *J. Phys. Chem. A* **2001**, *105* (41), 9396−9409.
(41) Chenoweth, K.; van Duin, A. C. T.; Goddard, W. A. ReaxFF reactive force field for molecular dynamics simulations of hydrocarbon oxidation. *J. Phys. Chem. A* **2008**, *112* (5), 1040−1053.
(42) *ReaxFF 2019, SCM, Theoretical Chemistry*; Vrije Universiteit: Amsterdam, The Netherlands, 2019, http://www.scm.com.
(43) Alfè, D. PHON: A program to calculate phonons using the small displacement method. *Comput. Phys. Commun.* **2009**, *180* (12), 2622−2633.
(44) Hjorth Larsen, A.; Jørgen Mortensen, J.; Blomqvist, J.; Castelli, I. E.; Christensen, R.; Dułak, M.; Friis, J.; Groves, M. N.; Hammer, B.; Hargus, C.; Hermes, E. D.; Jennings, P. C.; Bjerre Jensen, P.; Kermode, J.; Kitchin, J. R.; Leonhard Kolsbjerg, E.; Kubal, J.; Kaasbjerg, K.; Lysgaard, S.; Bergmann Maronsson, J.; Maxson, T.; Olsen, T.; Pastewka, L.; Peterson, A.; Rostgaard, C.; Schiøtz, J.; Schütt, O.; Strange, M.; Thygesen, K. S.; Vegge, T.; Vilhelmsen, L.; Walter, M.; Zeng, Z.; Jacobsen, K. W. The atomic simulation environment-a Python library for working with atoms. *J. Phys.: Condens. Matter.* **2017**, *29* (27), 273002.



https://doi.org/10.1021/acsnano.4c15300
*ACS Nano* 2025, 19, 2769−2776